Superconductivity in twisted bilayer WSe_2

Yiyu Xia[1*], Zhongdong Han[2*], Kenji Watanabe[3], Takashi Taniguchi[3], Jie Shan[1,2,4**], Kin Fai Mak[1,2,4**]

[1]School of Applied and Engineering Physics, Cornell University, Ithaca, NY, USA
[2]Laboratory of Atomic and Solid State Physics, Cornell University, Ithaca, NY, USA
[3]National Institute for Materials Science, Tsukuba, Japan
[4]Kavli Institute at Cornell for Nanoscale Science, Ithaca, NY, USA

*These authors contributed equally
* *Email: jie.shan@cornell.edu; kinfai.mak@cornell.edu

Moiré materials have enabled the realization of flat electron bands and quantum phases that are driven by strong correlations associated with flat bands[1-5]. Superconductivity has been observed, but solely, in graphene moiré materials[6-11]. The absence of robust superconductivity in moiré materials beyond graphene, such as semiconductor moiré materials[5], has remained a mystery and challenged our current understanding of superconductivity in flat bands. Here, we report the observation of robust superconductivity in both 3.5- and 3.65-degree twisted bilayer WSe_2 which hosts a hexagonal moiré lattice[12,13]. Superconductivity emerges at half-band filling and under small sublattice potential differences. The optimal superconducting transition temperature is about 200 mK in both cases, and constitutes about 1-2% of the effective Fermi temperature; the latter is comparable to the value in high-temperature cuprate superconductors[14,15] and suggests strong pairing. The superconductor borders on two distinct metals below and above half-band filling; it undergoes a continuous transition to a correlated insulator by tuning the sublattice potential difference. The observed superconductivity on the verge of Coulomb-induced charge localization suggests roots in strong electron correlations[14,16].

Main

The discovery of superconductivity in twisted bilayer graphene[6] has initiated intense research on moiré superlattices of van der Waals materials[1,2,4,5]. In particular, transition metal dichalcogenide (TMD) semiconductors, MX_2 (M = Mo, W; X = S, Se, Te), in the monolayer limit can be viewed as gapped graphene with strong Ising spin-orbit coupling[17]; TMD moiré materials have emerged as a simple yet extremely rich model system for studies of correlated and topological phases of matter[5]. The tunable moiré flat bands in these materials, which strongly enhance the correlation effects, have stabilized the Mott insulators[18-20], generalized Wigner crystals[18,21] and heavy fermions[22]. The combined correlation and non-trivial band topology have further induced the integer and fractional Chern insulators[23-28] and the fractional quantum spin Hall insulator[29], the latter of which has not been observed in any other materials. However, superconductivity—a hallmark of graphene flat band systems both with and without the moiré effects[6-11,30-34]—has remained elusive in TMD moiré materials. An earlier study reported the observation of a potential superconducting state in twisted bilayer WSe_2 ($tWSe_2$) by doping a correlated insulator[20], but the state appears unstable to repeated thermal cycles.

In this work, we report an electrical transport study of AA-stacked 3.5°- and 3.65°-$tWSe_2$. Results from the 3.65°- and 3.5°-device will be presented in the main text and in Extended Data Fig. 8, respectively. In both devices, we observe robust superconductivity on the verge of Coulomb-induced charge localization around half-band filling when the interlayer potential difference is tuned close to zero. The state borders on two distinct metals, below and above half-band filling, respectively. The superconducting transition temperature constitutes about 1-2% of the effective Fermi temperature, which is comparable to the value in cuprate high-temperature superconductors[14,15] and suggests strong pairing. The observed superconducting state does not stem from doping a correlated insulator and cannot be readily explained by the existing theories[35-49]. Future experiments and theories are required to fully understand the nature of the state.

Figure 1a illustrates a schematic of the dual-gated $tWSe_2$ device employed in this study. Twisted bilayer WSe_2 has a hexagonal moiré lattice with two sublattice sites residing at the MX and XM stacking regions[12,13] (Fig. 1b). The moiré density [n_M = $(4.25 \pm 0.03) \times 10^{12}\ \mathrm{cm}^{-2}$], or equivalently, the twist angle (3.65° ± 0.01°) is calibrated through quantum oscillations under a high magnetic field (Extended Data Fig. 2). The top and bottom gates are made of multilayer hexagonal boron nitride (hBN) and graphite. They independently tune the hole moiré filling factor ν and the electric field E perpendicular to $tWSe_2$ (or equivalently, the interlayer/sublattice potential difference). The narrower top gate defines the device channel and additional Pd split gates are patterned to turn off any parallel conduction channels. To achieve ohmic contacts to $tWSe_2$ down to mK temperatures, we use Pt contact electrodes and Pd contact gates. The contact gates induce heavy hole doping in the $tWSe_2$ regions immediately adjacent to the Pt electrodes. Contact resistance between 10-40 kΩ has been achieved (Extended Data Fig. 1). See Methods for details on the device fabrication, twist angle and disorder calibration and electrical measurements.

Figure 1c illustrates the electronic band structure for the first two moiré valence bands of 3.65°-$tWSe_2$ at $E = 0$, calculated using a reported continuum model[13] (Methods). The bands are composed of the spin-valley locked electronic state from the K or K' valley of monolayer WSe_2. Only the K-valley state is shown in Fig. 1c. Both moiré bands carry Chern number +1 (-1 for the K'-valley state), and are expected to transition to non-topological bands under a sufficiently high electric field that overcomes the interlayer hopping[12,13]. Figure 1d displays the corresponding electronic density of states (DOS) at the Fermi level as a function of E and ν. For $E = 0$, the DOS shows a van Hove singularity (vHS) near $\nu = 0.75$ which arises from a saddle point located at the m-point of the moiré Brillouin zone[20]. Across the vHS, the hole Fermi surface changes abruptly from disconnected κ/κ' hole pockets to a single γ electron pocket (insets). As E increases, the vHS shifts continuously towards higher ν (Extended Data Fig. 4) and exhibits a wing-like feature in the DOS.

Figure 1e shows the longitudinal resistance R measured as a function of E and ν (< 2) at 10 K. The map is dominated by a large resistance region that is centered around $E = 0$ and expands with increasing ν. Multiple correlated insulating states ($\nu = 1/4$, 1/3 and 1) can be identified. In line with earlier studies[12,13,24-27], this is the layer-hybridized region. The region at higher electric fields is characterized by a metallic state and is the layer-polarized region. Upon further cooling of the sample down to 50 mK (Fig. 1f), all the features become sharper, allowing us to draw the dashed lines to guide the eye for the phase boundary. The resistance maps in general show good agreement with the DOS map in Fig. 1d except at commensurate fillings ($\nu = 1/4$, 1/3 and 1), where the correlation effects dominate[21]. The enhanced resistance near $\nu = 0.75$ and $E = 0$ and at the wing-like features for $\nu > 1$ near the phase boundary follows closely the location of the calculated vHS (the enhanced resistance is presumably from the large DOS and/or enhanced scattering rate near the vHS). The assignment is further supported by a sign change of the Hall resistance (Extended Data Fig. 5). However, the most striking feature of Fig. 1f is the opening of a short strip with nearly vanishing resistance in the middle of the correlated insulator state at half-band filling ($\nu = 1$).

Superconductivity at half-band filling

We zoom in on the phase space near $\nu = 1$ and $E = 0$ in Fig. 2. The dashed lines are provided to guide the eye for the regions with zero resistance at 50 mK. Zero resistance is observed near the two ends of the $\nu = 1$ insulator (Fig. 2a). The zero-resistance state is independent of the measurement configuration for a homogenous moiré area of 1.5 μm × 8 μm (Extended Data Fig. 1 and 3). It is robust against repeated thermal cycles; over 10 thermal cycles were involved in collecting the data presented in the main text. On the other hand, the zero-resistance state is susceptible to both thermal excitations and magnetic field threaded through the sample. For instance, the state is quenched when the sample is warmed up to 300 mK (Fig. 2b) and when an out-of-plane magnetic field of 50 mT is applied at 50 mK (Fig. 2c). Figure 2 also shows that the zero-resistance state is not connected to the vHS near $\nu = 0.75$ and $E = 0$. It borders on two distinct metallic states, more discussions on which will follow in the next section.

For now, we focus on the zero-resistance state at the upper end of the insulator ($\nu \approx 1$ and $E \approx 8$ mV/nm) and examine its response to bias current I, temperature T and magnetic field B. Figure 3a displays the differential resistance, $\frac{dV}{dI}$, as a function of T and I in the absence of magnetic field. Linecuts at representative temperatures are illustrated in Fig. 3b. Below about 180 mK (dashed line in Fig. 3b), bias current above a critical value is required to destroy the zero-resistance state. The critical current is about 5 nA at 50 mK, and the value decreases monotonically with increasing temperature. Above about 250 mK, the differential resistance increases slightly with bias. Between the two temperatures, a resistance dip at zero bias is still observed although zero resistance is no longer reached. Figure 3c shows the temperature dependence of the differential resistance at zero bias, R. As temperature decreases, R first drops rapidly near 250 mK and then transitions to a zero-resistance state near 180 mK.

A similar study on the magnetic-field response is shown in Fig. 3d-f. Figure 3d displays the differential resistance, $\frac{dV}{dI}$, as a function of B and I at 50 mK (linecuts at representative magnetic fields are included in Extended Data Fig. 6d). Similar to Fig. 3a,b, the critical current required to destroy the zero-resistance state vanishes continuously with increasing magnetic field. The zero-resistance critical field, B_{C1}, is about 6 mT. Above this field, a resistance dip at zero bias is still observed and disappears in the normal state above the second critical field B_{C2}. Figure 3e shows the zero-bias resistance, R, as a function of T and B. Linecuts at representative magnetic fields are shown in Fig. 3f. At 50 mK, the normal state is reached at about 80 mT, above which R has a weak field dependence. Between the two critical fields, R increases linearly with field, and B_{C2} is defined as the field at which the linear fits to the field dependence of R in two different phases intersect (Extended Data Fig. 6c). The critical fields are evaluated for all temperatures (filled symbols, Fig. 3e). They vanish continuously at the corresponding transition temperatures.

The results above are fully consistent with superconductivity in two dimensions (2D). Because of the enhanced thermal fluctuations, the superconducting transition in 2D is expected to occur over a temperature range[50], characterized by the onset of Cooper pairing at the pairing temperature, T_P, and the onset of quasi-long-range phase coherence at the Berezinskii-Kosterlitz-Thouless (BKT) transition temperature, T_{BKT}. We define T_P (≈ 250 mK) as the temperature at which the zero-bias resistance reaches 80% of the normal-state resistance (Extended Data Fig. 6a). We determine T_{BKT} (≈ 180 mK) by performing the BKT analysis (inset of Fig. 3c), that is, the nonlinear $I - V$ dependence takes the form $V \propto I^3$ (dashed line) at T_{BKT} (Ref. [50,51]).

The observed broad superconducting transition induced by magnetic fields is also expected for weakly pinned vortices. Here B_{C1} and B_{C2} correspond to the critical fields, at which the zero-resistance state and Cooper pairing with finite resistance are destroyed, respectively. The observed $R \propto \frac{B}{B_{C2}}$ (Extended Data Fig. 6c) between the two critical fields is consistent with nearly unpinned vortices in the superconductor[50]. Such mobile vortices have been reported in 2D crystalline superconductors with shallow pinning sites[51]. Our high-quality $tWSe_2$ device with low disorder density (about 2.5% of the moiré density n_M, Extended Data Fig. 1) is compatible with this picture. We can estimate the superconducting coherence length ξ by fitting the Ginzburg-Landau result $B_{C2} \approx \frac{\Phi_0}{2\pi\xi^2}\left(1 - \frac{T}{T_P}\right)$ to the experimental temperature dependence of B_{C2} near T_P (dashed line in Fig. 3e, Ref. [50]). Here $\Phi_0 = h/2e$ is the flux quantum with h and e denoting the Planck constant and fundamental charge, respectively. The superconducting coherence length ($\xi \approx 52$ nm) is about 10 times the moiré period ($a_M \approx 5$ nm).

Doping dependence of the superconductor

We examine the doping dependence of the superconducting state, focusing on the upper end of the insulator (Fig. 2a, $E \approx 8$ mV/nm) as above. Figure 4a shows zero-bias resistance, R, as a function of T and ν in the absence of magnetic fields. Linecuts at representative temperatures are shown in Fig. 4b. Superconductivity is observed only in the immediate vicinity of $\nu = 1$. The pairing and BKT transition temperatures are shown as blue and orange symbols in Fig. 4a, respectively. The optimal T_{BKT} is slightly below 200 mK at $\nu \approx 1$.

The state on both sides of the superconductor is metallic. Figure 4c illustrates the temperature dependence of R at three representative filling factors, $\nu = 0.9$, 1 and 1.1. Figure 4d displays R as a function of T^2. The metallic state above filling one shows a Fermi liquid behavior with $R = R_0 + AT^2$ (dashed line, Fig. 4d) over an extended temperature range in the low-temperature limit. Here R_0 is the residual resistance and A is the Kadowaki-Woods coefficient that reflects the quasiparticle effective mass[52]. We define coherence temperature, T_{coh}, as the crossover temperature at which R deviates from the Fermi liquid behavior by 10% (Extended Data Fig. 11 shows a similar trend using 20% threshold). As filling factor approaches one from above, T_{coh} rapidly decreases (Fig. 4a), and correspondingly, A or the quasiparticle effective mass rapidly increases (inset of Fig. 4d).

On the other hand, the metallic state below filling one and the normal state of the superconductor are not compatible with a Fermi liquid for nearly the entire temperature window and T_{coh} cannot be reliably extracted. The normal state of the superconductor at $\nu = 1$ also exhibits a resistance peak at elevated temperature T^* (Fig. 4b,c). This temperature scale separates the coherent and incoherent transport regimes (below and above T^*, respectively) and can be used as a measure of the Fermi temperature, T_F (Ref. [53]). We illustrate T^* as yellow symbols in Fig. 4a for all filling factors that can be identified within the measurement window of 25 K. It reaches a minimum of about 10 K at $\nu = 1$, which is substantially suppressed compared to the single-particle $T_F \gtrsim 100$ K from the band structure calculation in Fig. 1c (see Methods for additional estimates). The result shows that the normal state of the superconductor is developed from a poor metal with the lowest T_F, one that is on the verge of charge localization induced by the strong electronic correlation at $\nu = 1$. (Note that the Fermi liquid behavior for $\nu > 1$ is developed only for $T < T_{coh} < T^*$.)

Superconductor-insulator transition

The proximity to charge localization of the normal state of the superconductor is further supported by the superconductor-insulator transition induced by out-of-plane electric field E at $\nu = 1$. Figure 5a shows zero-bias resistance, R, as a function of T and E with linecuts at representative electric fields shown in Fig. 5b. All resistance curves merge into the same temperature dependence above about 4 K (see Fig. 1e for a wider E-field range at 10 K). A sharp superconductor-insulator transition is observed near the critical electric field $E_C \approx 11.7$ mV/nm. The corresponding resistance R_C (dashed line in Fig. 5b) has the weakest temperature dependence.

Figure 5c demonstrates the collapse of the resistance curves in the vicinity of E_C. In this process, we first extract the thermal activation gap T_0 of the insulating state at each E (Extended Data Fig. 7). The activation gap (black symbols, Fig. 5a) vanishes continuously as E approaches E_C from above. The normalized resistance R/R_C for all fields collapses into two groups of curves if we scale the temperature axis by T_0. For the superconducting side, the same T_0 as its insulating counterpart that lies with equal distance to E_C gives the best scaling. One group of the collapsed curves decreases, and the other group diverges, with decreasing T/T_0. In Fig. 5a, we also show the electric-field dependence of T_{BKT} and T_P on the superconducting side. Both temperature scales vanish continuously as E approaches E_C from below. The continuously vanishing temperature/energy scales and the collapse of the resistance curves in the vicinity of E_C suggest that the superconductor-insulator transition is a continuous electric-field-induced quantum phase transition.

Concluding remarks

We have observed robust superconductivity in both 3.5°- and 3.65°-twisted bilayer WSe_2. The observed superconducting state has several unusual properties that deserve future studies. First, superconductivity is observed only in the layer-hybridized region of the twisted bilayer[12,13,24-27] (Fig. 1f). The TMD moiré system with tunable bands in this regime is an excellent platform to investigate the role of quantum geometry in superconductivity[54]. Second, superconductivity is strongly confined near $\nu = 1$ and is away from the vHS (at $\nu \approx 0.75$ near $E = 0$). The superconductor evolves continuously to a correlated insulator by tuning the interlayer potential difference (Fig 2 and 5). The phenomenology is different from that in graphene moiré systems, where superconductivity emerges often by doping a correlated insulator[6-11]. Third, the normal state of the superconductor is a strongly correlated metal with minimal $T_F \approx T^*$ on the verge of localization (Fig. 4). The superconducting state borders on two distinct metallic states: a well-behaved Fermi liquid above filling one and one that largely deviates from the Fermi-liquid behavior below filling one. These metallic states are not spontaneously spin/valley-polarized (Extended Data Fig. 5), also distinct from the phenomenology of superconductivity in bilayer and trilayer graphene[31,33,34,55]. Finally, the observed superconductor is in the strong pairing limit with T_C (superconducting transition temperature) about 1-2% of T_F and ξ about 10 times a_M or the inter-particle distance at $\nu = 1$ (see Methods for additional estimates). These values are comparable to the ratios $\frac{T_C}{T_F}$ and $\frac{\xi}{a}$ in high-T_C cuprates[14,56] (a is the lattice constant). Transport experiments on samples with other twist angles and different TMDs, as well as magnetic circular dichroism measurements, could help to address questions such as the nature of the correlated insulator[57,58] and the normal metallic states surrounding the superconductor. Direct demonstration of the Josephson effect is also desired. Our experiment opens the door to explore unconventional superconductivity driven by strong electronic correlations in semiconductors moiré materials.

Methods

Device fabrication.

Extended Data Fig. 1a shows a schematic representation of dual-gated $tWSe_2$ devices. They were fabricated using the 'tear-and stack' and layer-by-layer dry transfer method, as described in previous studies[6,59]. In short, flakes of few-layer graphite, multilayer hexagonal Boron Nitride (hBN) and monolayer WSe_2 were first exfoliated from bulk crystals onto Si/SiO_2 substrates and identified based on their optical reflection contrast. The WSe_2 flake was cut into two halves using an AFM (atomic force microscope) tip. The flakes were then picked up sequentially by a polycarbonate thin film on a PDMS (polydimethylsiloxane) stamp in the following order: hBN, top-gate graphite, hBN, one half of the WSe_2 flake, second half of the WSe_2 flake with a twist, hBN and bottom-gate graphite. The top and bottom gate hBN thickness is 2.9 nm and 6.1 nm, respectively, for the 3.65° device and 3.6 nm and 5.6 nm, respectively, for the 3.5° device. Since the hBN thickness is comparable to the moiré period (about 5 nm), we expect the extended-range (on-site) Coulomb repulsion is substantially (weakly) screened. The complete stack was subsequently released onto a Si/SiO_2 substrate with pre-patterned Pt electrodes in the Hall bar geometry at 200°C. Finally, the contact gates and the split gates were added using standard electron-beam lithography and evaporation of Ti/Pd (5 nm/40 nm in thickness). The top gate is smaller than the bottom gate in area and defines the device channel. The contact gates serve to heavily hole-dope the $tWSe_2$ regions between the channel and the Pt electrodes to reduce the contact resistance (even when the doping density in the channel is low). The split gates are used to deplete the parallel $tWSe_2$ regions that are gated only by the bottom gate. An optical micrograph of the 3.65° device is shown in Extended Data Fig. 1b.

Compared to earlier $tWSe_2$ devices[20,60], we have achieved 1) better contacts for transport measurements down to mK temperatures, 2) an improved design of the dual-gated device allowing mapping of the entire electrostatics phase diagram and 3) reduced moiré inhomogeneity to about 2-3% of the moiré density over a large channel area. These advancements enable the observation of robust superconductivity in this study.

Electrical measurements.

The electrical transport measurements were performed in a dilution refrigerator (Bluefors LD250) equipped with a 12 T superconducting magnet. Low-temperature RC and RF filters (QDevil) were installed on the mixing chamber plate to filter out the electrical noise from about 65 kHz to tens of GHz. A 1 MΩ resistor was added in series to limit the excitation current. Voltage pre-amplifiers with large input impedance (100 MΩ) were used to measure sample resistances up to about 10 MΩ. Low-frequency (5.777 Hz) lock-in techniques were adapted to measure the sample resistance with a small excitation current (< 10 nA) to avoid sample heating. Specifically, the excitation current was fixed below 1 nA to probe the superconducting state. Both the voltage drop at the probe electrodes and the source-drain current were recorded. All data were taken at the base temperature (~ 50 mK) unless specified otherwise.

Twist angle calibration.

The twist angle of WSe_2 was calibrated through the quantum oscillations observed under a perpendicular magnetic field. We first acquired a resistance map under zero magnetic field as a function of the top gate and bottom gate voltages (V_{tg} and V_{bg}, respectively). We converted the gate voltages to a perpendicular electrical field, $E = \frac{1}{2}\left(\frac{V_{bg}}{d_{bg}} - \frac{V_{tg}}{d_{tg}}\right)$, and filling factor, $\nu \propto \frac{V_{bg}}{d_{bg}} + \frac{V_{tg}}{d_{tg}}$, using the hBN thickness in the top and bottom gates (d_{tg} and d_{bg}, respectively). The hBN thicknesses were independently calibrated by AFM, and their ratio was fine-tuned to align the resistance peaks parallel to the electric-field axis (Extended Data Fig. 2a). The two most prominent resistance peaks are insulating states at $\nu = 1$ and $\nu = 2$. Using the same thickness values, we also obtained the resistance map at 12 T as a function of E and ν (Extended Data Fig. 2b). Landau levels are observed. We focus on the layer-polarized region under large electric fields, where the Landau levels are spin- and valley-polarized akin to that in hole-doped monolayer WSe_2 under large magnetic fields[61]. Landau levels with index $\nu_{LL} = 2 - 8$ are denoted by vertical dashed lines, and their filling dependence is shown in Extended Data Fig. 2c. We determined the moiré density, $n_M = (4.25 \pm 0.03) \times 10^{12}\ \mathrm{cm}^{-2}$, from the slope ($\frac{\phi_0}{B} n_M$ with $\phi_0 = \frac{h}{e}$ denoting the magnetic flux quantum) of the best linear fit to the experimental data. We obtained the twist angle, $\theta = a\sqrt{\frac{\sqrt{3}}{2} n_M} = 3.65° \pm 0.01°$ from the moiré density, where $a \approx 3.317$ Å (Ref. [62]) is the lattice constant of monolayer WSe_2. The twist angle can also be determined from the Landau fans emerging from the moiré band edges (Extended Data Fig. 2d). Here clear Landau levels emerging from $\nu = 0$ and 2 can be identified, from which a nearly identical twist angle can be obtained.

We can further determine the twist angle using the Hofstadter's oscillations. Extended Data Fig. 2e shows the density derivative of the sample conductance versus $1/B$ and ν. Periodic crossings of the Landau levels at a period $0.0058 \pm 0.0001\ \mathrm{T}^{-1}$ are observed under high magnetic fields when the magnetic length becomes comparable to the moiré period. According to the Hofstadter's butterfly model, this period is $\frac{1}{B} = \frac{q}{\phi_0 n_M}$ (q is an integer), which is plotted in Extended Data Fig. 2f. We then obtain a moiré density $n_M \approx (4.22 \pm 0.06) \times 10^{12}\ \mathrm{cm}^{-2}$ and a twist angle $\theta = 3.63° \pm 0.03°$. The result is fully consistent with the above value and is consistent with the targeted twist angle in the fabrication process (within 0.2°).

Band structure calculation.

To capture the low-energy electronic band structure of $tWSe_2$ of small twist angle, we study the continuum model based on the effective mass description first introduced by Wu *et al.* (Ref. [12]). In monolayer TMDs, the topmost valence bands are spin split by 100's meV and the spin and valley are locked due to inversion symmetry breaking and strong spin-orbit coupling (Ref. [17]). This property is inherited by $tWSe_2$. For each valley, the low-energy physics of $tWSe_2$ can be described by a two-band $k \cdot p$ model with a periodic pseudomagnetic field, $\Delta(\boldsymbol{r}) = (\mathrm{Re}\Delta_T^\dagger, \mathrm{Im}\Delta_T^\dagger, \frac{\Delta_b - \Delta_t}{2})$, where Δ_T is the interlayer tunneling amplitude and $\Delta_{b,t}$ are the bottom and top layer dependent energies. The effective moiré Hamiltonian for the $+K$ valley state (with spin-↑) is given by

$$H_\uparrow = \begin{pmatrix} -\frac{\hbar^2(k-\kappa_+)^2}{2m^*} + \Delta_b(\boldsymbol{r}) & \Delta_T(\boldsymbol{r}) \\ \Delta_T^\dagger(\boldsymbol{r}) & -\frac{\hbar^2(k-\kappa_-)^2}{2m^*} + \Delta_t(\boldsymbol{r}) \end{pmatrix}, \tag{1}$$

where m^* is the valence band effective mass ($= 0.45m_0$ for monolayer WSe_2 [Ref. [63]]) and $\kappa_\pm$ are the corners of the moiré Brillouin zone (mBZ). The effective Hamiltonian for the $-K$ valley state (with spin-↓) is the complex conjugate of $H_\uparrow$.

The pseudomagnetic field with the lattice symmetry constraints can be described in the lowest harmonic approximation as

$$\Delta_{b,t}(\boldsymbol{r}) = \pm\frac{V_z}{2} + 2V\sum_{j=1,3,5}\cos(\mathbf{g}_{\boldsymbol{j}}\cdot\boldsymbol{r}\pm\psi), \tag{2}$$

$$\Delta_T(\boldsymbol{r}) = w(1 + e^{-i\mathrm{g}_2\cdot\boldsymbol{r}} + e^{-i\mathrm{g}_3\cdot\boldsymbol{r}}). \tag{3}$$

Here V_z denotes the sublattice potential difference and $\mathbf{g}_{\boldsymbol{j}}$ is the reciprocal lattice vector obtained by counterclockwise rotations of $\mathbf{g}_{\mathbf{1}} = (\frac{4\pi}{\sqrt{3}a_M}, 0)$ by angle $(j-1)\pi/3$. The parameters $(V,\ \psi,\ w) = (9.0\text{ meV},\ 128°,\ 18\text{ meV})$ are taken from the DFT (density functional theory) calculations for $tWSe_2$ (Ref. [13]).

We obtain the band structure and density of states (DOS) by diagonalizing the Hamiltonian given in Eq. (1). The result for 3.65°-twisted WSe_2 (as studied in the experiment) is shown in Fig. 1c,d. To compare with experiment, we convert the sublattice potential difference to vertical electric field using $E = V_z/(\frac{\varepsilon_{hBN}}{\varepsilon_{TMD}}et)$. Here the dipole moment $\frac{\varepsilon_{hBN}}{\varepsilon_{TMD}}et \approx 0.26\, e\cdot nm$ is independently determined from the anti-crossing feature of the layer-hybridized moiré excitons[64,65] ($\varepsilon_{hBN} \approx 3$ and $\varepsilon_{TMD} \approx 8$ are the out-of-plane dielectric constants of hBN and TMD, respectively, and $t \approx 0.7\, nm$ is the interlayer separation between the WSe_2 monolayers).

Estimate of superconductor properties.
We estimate the ratio $\frac{T_C}{T_F}$ for superconducting $tWSe_2$ at $\nu > 1$, where T_C and T_F are the superconducting transition temperature and the Fermi temperature, respectively. We use the mean of the pairing and BKT transition temperatures to represent $T_C \approx \frac{T_{BKT}+T_P}{2} \approx$ 220 mK and use $T^* \approx 10$ K to approximate T_F. The estimated value $\frac{T_C}{T_F} \approx 0.02$ suggests strong pairing and is comparable to that in high-T_C cuprates[14]. The strong pairing is further evidenced by the ratio $\frac{\xi}{a_M} \approx 10$, where $a_M \approx 5$ nm is the moiré period and $\xi \approx 52$ nm is the superconducting coherence length extracted from the critical magnetic-field measurement (Fig. 3e). The equivalent value for cuprates is about 5 (Ref. [56]).

We can also estimate Fermi velocity $v_F \approx \frac{\xi k_B T_C}{\hbar} \approx 1{,}500$ m/s and effective quasiparticle mass $m \approx \frac{\hbar^2\pi n_M}{k_B T_F} \approx 10\, m_0$ at the Fermi level, where k_B, $\hbar$ and m_0 denote the Boltzmann constant, reduced Planck's constant and the free electron mass, respectively. The obtained values are self-consistent with the relation $mv_F = \hbar\sqrt{2\pi n_M}$. Both m and v_F are strongly renormalized from their single-particle values based on the continuum model[12,13] (Fig. 1c).

Lastly, we can estimate an effective $T_F \sim \frac{\hbar v_F k_F}{k_B} = \sqrt{\frac{4\pi}{\sqrt{3}}} \frac{\xi}{a_M} T_C \approx 6$ K using $\xi = \frac{\hbar v_F}{k_B T_C} \approx 52$ nm, $T_C \approx 220$ mK and the Fermi momentum $k_F = \sqrt{\frac{4\pi}{\sqrt{3}}} \frac{1}{a_M}$. The estimated value is in good agreement with the measured $T^* \approx 10$ K.

Acknowledgements

We thank B. A. Bernevig, D. Chowdhury, S. Das Sarma, L. Fu, C. Jian, E.-A. Kim, K. T. Law, A. H. MacDonald and Q. Si for helpful discussions. We also thank J. Zhu and P. Knüppel for many technical discussions.

References

1 Andrei, E. Y. & MacDonald, A. H. Graphene bilayers with a twist. *Nature materials* **19**, 1265-1275 (2020).
2 Balents, L., Dean, C. R., Efetov, D. K. & Young, A. F. Superconductivity and strong correlations in moiré flat bands. *Nature Physics* **16**, 725-733 (2020).
3 Andrei, E. Y. *et al.* The marvels of moiré materials. *Nature Reviews Materials* **6**, 201-206 (2021).
4 Kennes, D. M. *et al.* Moiré heterostructures as a condensed-matter quantum simulator. *Nature Physics* **17**, 155-163 (2021).
5 Mak, K. F. & Shan, J. Semiconductor moiré materials. *Nature Nanotechnology* **17**, 686-695 (2022).
6 Cao, Y. *et al.* Unconventional superconductivity in magic-angle graphene superlattices. *Nature* **556**, 43-50 (2018).
7 Lu, X. *et al.* Superconductors, orbital magnets and correlated states in magic-angle bilayer graphene. *Nature* **574**, 653-657 (2019).
8 Yankowitz, M. *et al.* Tuning superconductivity in twisted bilayer graphene. *Science* **363**, 1059-1064 (2019).
9 Arora, H. S. *et al.* Superconductivity in metallic twisted bilayer graphene stabilized by WSe2. *Nature* **583**, 379-384 (2020).
10 Park, J. M., Cao, Y., Watanabe, K., Taniguchi, T. & Jarillo-Herrero, P. Tunable strongly coupled superconductivity in magic-angle twisted trilayer graphene. *Nature* **590**, 249-255 (2021).
11 Hao, Z. *et al.* Electric field–tunable superconductivity in alternating-twist magic-angle trilayer graphene. *Science* **371**, 1133-1138 (2021).
12 Wu, F., Lovorn, T., Tutuc, E., Martin, I. & MacDonald, A. Topological insulators in twisted transition metal dichalcogenide homobilayers. *Physical review letters* **122**, 086402 (2019).
13 Devakul, T., Crépel, V., Zhang, Y. & Fu, L. Magic in twisted transition metal dichalcogenide bilayers. *Nature communications* **12**, 6730 (2021).
14 Uemura, Y. Condensation, excitation, pairing, and superfluid density in high-Tc superconductors: the magnetic resonance mode as a roton analogue and a possible spin-mediated pairing. *Journal of Physics: Condensed Matter* **16**, S4515 (2004).

15 Qijin Chen, Z. W., Rufus Boyack, Shuolong Yang, K. Levin. When Superconductivity Crosses Over: From BCS to BEC. *arXiv:2208.01774* (2023).
16 Lee, P. A., Nagaosa, N. & Wen, X.-G. Doping a Mott insulator: Physics of high-temperature superconductivity. *Reviews of Modern Physics* **78**, 17-85 (2006).
17 Xiao, D., Liu, G.-B., Feng, W., Xu, X. & Yao, W. Coupled spin and valley physics in monolayers of MoS 2 and other group-VI dichalcogenides. *Physical review letters* **108**, 196802 (2012).
18 Regan, E. C. *et al.* Mott and generalized Wigner crystal states in WSe2/WS2 moiré superlattices. *Nature* **579**, 359-363 (2020).
19 Tang, Y. *et al.* Simulation of Hubbard model physics in WSe2/WS2 moiré superlattices. *Nature* **579**, 353-358 (2020).
20 Wang, L. *et al.* Correlated electronic phases in twisted bilayer transition metal dichalcogenides. *Nature materials* **19**, 861-866 (2020).
21 Xu, Y. *et al.* Correlated insulating states at fractional fillings of moiré superlattices. *Nature* **587**, 214-218 (2020).
22 Zhao, W. *et al.* Gate-tunable heavy fermions in a moiré Kondo lattice. *Nature* **616**, 61-65 (2023).
23 Li, T. *et al.* Quantum anomalous Hall effect from intertwined moiré bands. *Nature* **600**, 641-646 (2021).
24 Cai, J. *et al.* Signatures of fractional quantum anomalous Hall states in twisted MoTe2. *Nature* **622**, 63-68 (2023).
25 Zeng, Y. *et al.* Thermodynamic evidence of fractional Chern insulator in moiré MoTe2. *Nature* **622**, 69-73 (2023).
26 Park, H. *et al.* Observation of fractionally quantized anomalous Hall effect. *Nature* **622**, 74-79 (2023).
27 Xu, F. *et al.* Observation of integer and fractional quantum anomalous Hall effects in twisted bilayer MoTe 2. *Physical Review X* **13**, 031037 (2023).
28 Foutty, B. A. *et al.* Mapping twist-tuned multiband topology in bilayer WSe2. *Science* **384**, 343-347 (2024).
29 Kang, K. *et al.* Evidence of the fractional quantum spin Hall effect in moiré MoTe2. *Nature* **628**, 522-526 (2024).
30 Oh, M. *et al.* Evidence for unconventional superconductivity in twisted bilayer graphene. *Nature* **600**, 240-245 (2021).
31 Zhou, H., Xie, T., Taniguchi, T., Watanabe, K. & Young, A. F. Superconductivity in rhombohedral trilayer graphene. *Nature* **598**, 434-438 (2021).
32 Kim, H. *et al.* Evidence for unconventional superconductivity in twisted trilayer graphene. *Nature* **606**, 494-500 (2022).
33 Zhou, H. *et al.* Isospin magnetism and spin-polarized superconductivity in Bernal bilayer graphene. *Science* **375**, 774-778 (2022).
34 Zhang, Y. *et al.* Enhanced superconductivity in spin–orbit proximitized bilayer graphene. *Nature* **613**, 268-273 (2023).
35 Hsu, Y.-T., Vaezi, A., Fischer, M. H. & Kim, E.-A. Topological superconductivity in monolayer transition metal dichalcogenides. *Nature Communications* **8**, 14985 (2017).

36 Venderley, J. & Kim, E.-A. Density matrix renormalization group study of superconductivity in the triangular lattice Hubbard model. *Physical Review B* **100**, 060506 (2019).
37 Slagle, K. & Fu, L. Charge transfer excitations, pair density waves, and superconductivity in moiré materials. *Physical Review B* **102**, 235423 (2020).
38 Schrade, C. & Fu, L. Nematic, chiral and topological superconductivity in transition metal dichalcogenides. *arXiv preprint arXiv:2110.10172* (2021).
39 Hsu, Y.-T., Wu, F. & Das Sarma, S. Spin-valley locked instabilities in moir\'e transition metal dichalcogenides with conventional and higher-order Van Hove singularities. *Physical Review B* **104**, 195134 (2021).
40 Bélanger, M., Fournier, J. & Sénéchal, D. Superconductivity in the twisted bilayer transition metal dichalcogenide WSe 2: A quantum cluster study. *Physical Review B* **106**, 235135 (2022).
41 Scherer, M. M., Kennes, D. M. & Classen, L. Chiral superconductivity with enhanced quantized Hall responses in moiré transition metal dichalcogenides. *npj Quantum Materials* **7**, 100 (2022).
42 Chen, F. & Sheng, D. Singlet, triplet, and pair density wave superconductivity in the doped triangular-lattice moiré system. *Physical Review B* **108**, L201110 (2023).
43 Crépel, V., Guerci, D., Cano, J., Pixley, J. & Millis, A. Topological superconductivity in doped magnetic moiré semiconductors. *Physical review letters* **131**, 056001 (2023).
44 Klebl, L., Fischer, A., Classen, L., Scherer, M. M. & Kennes, D. M. Competition of density waves and superconductivity in twisted tungsten diselenide. *Physical Review Research* **5**, L012034 (2023).
45 Wu, Y.-M., Wu, Z. & Yao, H. Pair-density-wave and chiral superconductivity in twisted bilayer transition metal dichalcogenides. *Physical Review Letters* **130**, 126001 (2023).
46 Zegrodnik, M. & Biborski, A. Mixed singlet-triplet superconducting state within the moiré t− J− U model applied to twisted bilayer WSe 2. *Physical Review B* **108**, 064506 (2023).
47 Zhou, B. & Zhang, Y.-H. Chiral and nodal superconductors in the t− J model with valley contrasting flux on a triangular moiré lattice. *Physical Review B* **108**, 155111 (2023).
48 Xie, Y.-M. & Law, K. Orbital Fulde-Ferrell pairing state in moiré Ising superconductors. *Physical Review Letters* **131**, 016001 (2023).
49 Akbar, W., Biborski, A., Rademaker, L. & Zegrodnik, M. Topological superconductivity with mixed singlet-triplet pairing in moir\'e transition-metal-dichalcogenide bilayers. *arXiv preprint arXiv:2403.05903* (2024).
50 Tinkham, M. *Introduction to superconductivity*. (Courier Corporation, 2004).
51 Saito, Y., Nojima, T. & Iwasa, Y. Highly crystalline 2D superconductors. *Nature Reviews Materials* **2**, 1-18 (2016).
52 Kadowaki, K. & Woods, S. B. Universal relationship of the resistivity and specific heat in heavy-Fermion compounds. *Solid State Communications* **58**, 507-509 (1986).

53 Smidman, M. *et al.* Colloquium: Unconventional fully gapped superconductivity in the heavy-fermion metal ${\mathrm{CeCu}}_{2}{\mathrm{Si}}_{2}$. *Reviews of Modern Physics* **95**, 031002 (2023).
54 Törmä, P., Peotta, S. & Bernevig, B. A. Superconductivity, superfluidity and quantum geometry in twisted multilayer systems. *Nature Reviews Physics* **4**, 528-542 (2022).
55 Chou, Y.-Z., Wu, F. & Das Sarma, S. Enhanced superconductivity through virtual tunneling in Bernal bilayer graphene coupled to ${\mathrm{WSe}}_{2}$. *Physical Review B* **106**, L180502 (2022).
56 Mourachkine, A. *High-Temperature Superconductivity in Cuprates: The Nonlinear Mechanism and Tunneling Measurements*. (Kluwer Academic Publishers, 2002).
57 Pan, H., Wu, F. & Das Sarma, S. Band topology, Hubbard model, Heisenberg model, and Dzyaloshinskii-Moriya interaction in twisted bilayer ${\mathrm{WSe}}_{2}$. *Physical Review Research* **2**, 033087 (2020).
58 Bi, Z. & Fu, L. Excitonic density wave and spin-valley superfluid in bilayer transition metal dichalcogenide. *Nature Communications* **12**, 642 (2021).
59 Wang, L. *et al.* One-dimensional electrical contact to a two-dimensional material. *Science* **342**, 614-617 (2013).
60 Ghiotto, A. *et al.* Quantum criticality in twisted transition metal dichalcogenides. *Nature* **597**, 345-349 (2021).
61 Gustafsson, M. V. *et al.* Ambipolar Landau levels and strong band-selective carrier interactions in monolayer WSe2. *Nature Materials* **17**, 411-415 (2018).
62 Mounet, N. *et al.* Two-dimensional materials from high-throughput computational exfoliation of experimentally known compounds. *Nature Nanotechnology* **13**, 246-252 (2018).
63 Fallahazad, B. *et al.* Shubnikov--de Haas Oscillations of High-Mobility Holes in Monolayer and Bilayer ${\mathrm{WSe}}_{2}$: Landau Level Degeneracy, Effective Mass, and Negative Compressibility. *Physical Review Letters* **116**, 086601 (2016).
64 Li, T. *et al.* Continuous Mott transition in semiconductor moiré superlattices. *Nature* **597**, 350-354 (2021).
65 Tang, Y. *et al.* Tuning layer-hybridized moiré excitons by the quantum-confined Stark effect. *Nature Nanotechnology* **16**, 52-57 (2021).

Figures

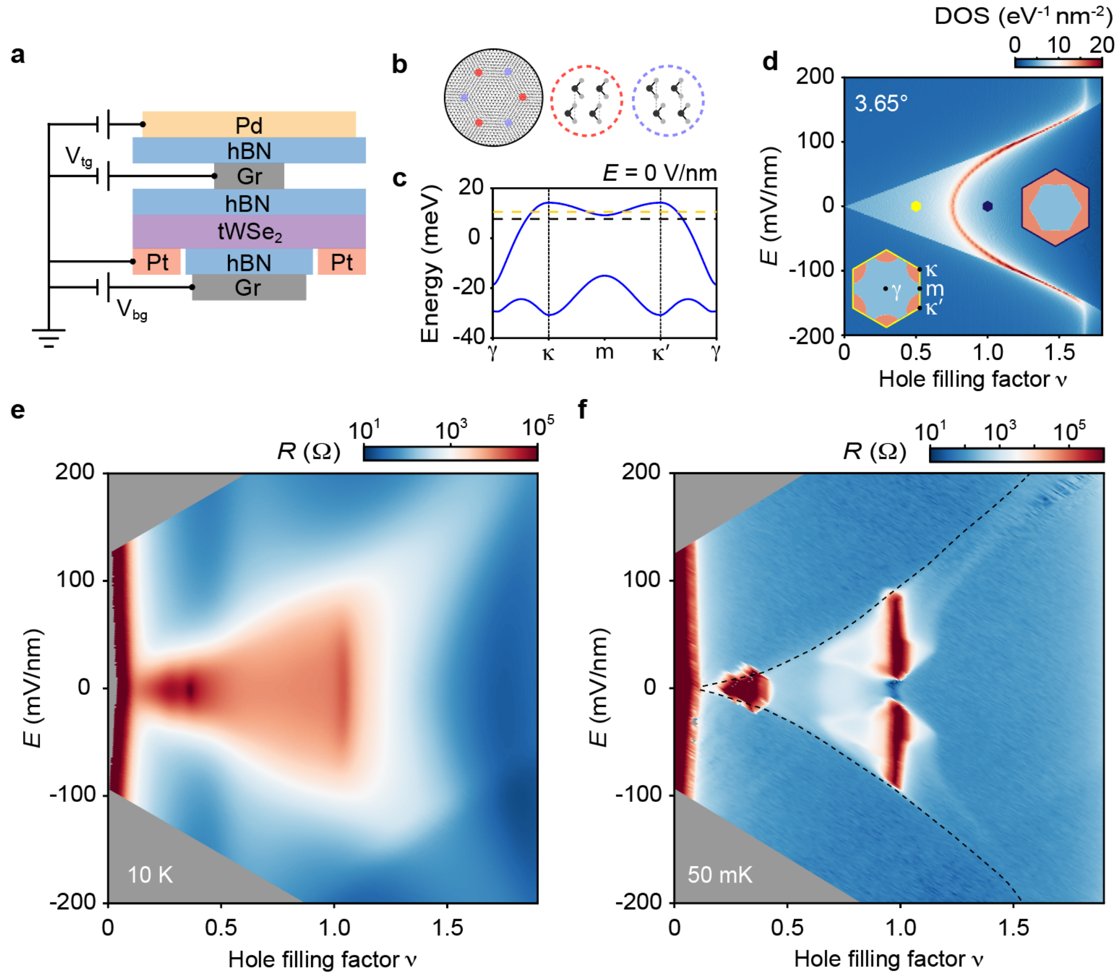

Figure 1 | Electronic structure of $tWSe_2$. a, Schematic of a dual-gated $tWSe_2$ device. Both gates are made of hBN and few-layer graphite (Gr) with the narrower top gate defining the $tWSe_2$ channel. The top and bottom gate voltages (V_{tg} and V_{bg}, respectively) control the vertical electric field E and hole filling factor ν in $tWSe_2$. Platinum (Pt) is the contact electrodes to $tWSe_2$. Additional palladium (Pd) contact gate and split gate voltages turn on the Pt contacts and turn off the parallel channels, respectively (only one gate is shown). **b,** Hexagonal moiré lattice of $tWSe_2$ with sublattice sites centered at the MX (red) and XM (blue) stacking sites; black and grey dots denote the M (= W) and X (= Se) atoms, respectively. **c,** Topmost moiré valence bands for the K-valley state of 3.65°-$tWSe_2$ from the continuum model. Both bands carry Chern number +1. The corresponding bands of the K'-valley state carry Chern number -1. The valence band maximum at 14.2 meV corresponds to $\nu = 0$. The dashed lines mark the Fermi levels corresponding to the dots of the same color in **d**. **d,** Electronic density of states (DOS) versus E and ν. The vHS ($\nu \approx 0.75$ at $E = 0$) disperses towards higher ν with increasing E. Insets: Fermi surface at $E = 0$ evolves from disconnected hole pockets centered at κ/κ' of the moiré Brillouin zone (yellow) to a single electron pocket centered at γ (black) as ν passes the vHS. **e,f,** Longitudinal resistance R as a function of E and ν at 10 K (**e**) and 50 mK (**f**). The dashed lines in **f** (a guide to the eye) separate the layer-hybridized and layer-polarized regions.

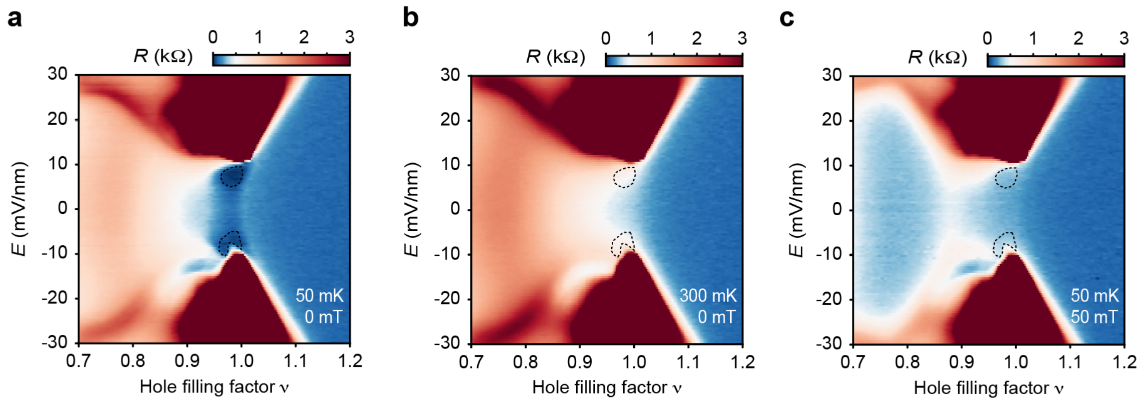

Figure 2 | Zero-resistance region around half-band filling. a-c, Longitudinal resistance R as a function of E and ν near $E = 0$ and $\nu = 1$ at different temperatures and externally applied magnetic fields. The dotted lines are a guide to the eye of the zero-resistance region observed at 50 mK (**a**). The zero-resistance state is quenched by increasing the sample temperature to 300 mK (**b**) or by applying an out-of-plane magnetic field of 50 mT (**c**). The metallic states immediately below and above half-band filling are insensitive to the magnetic field in **c**.

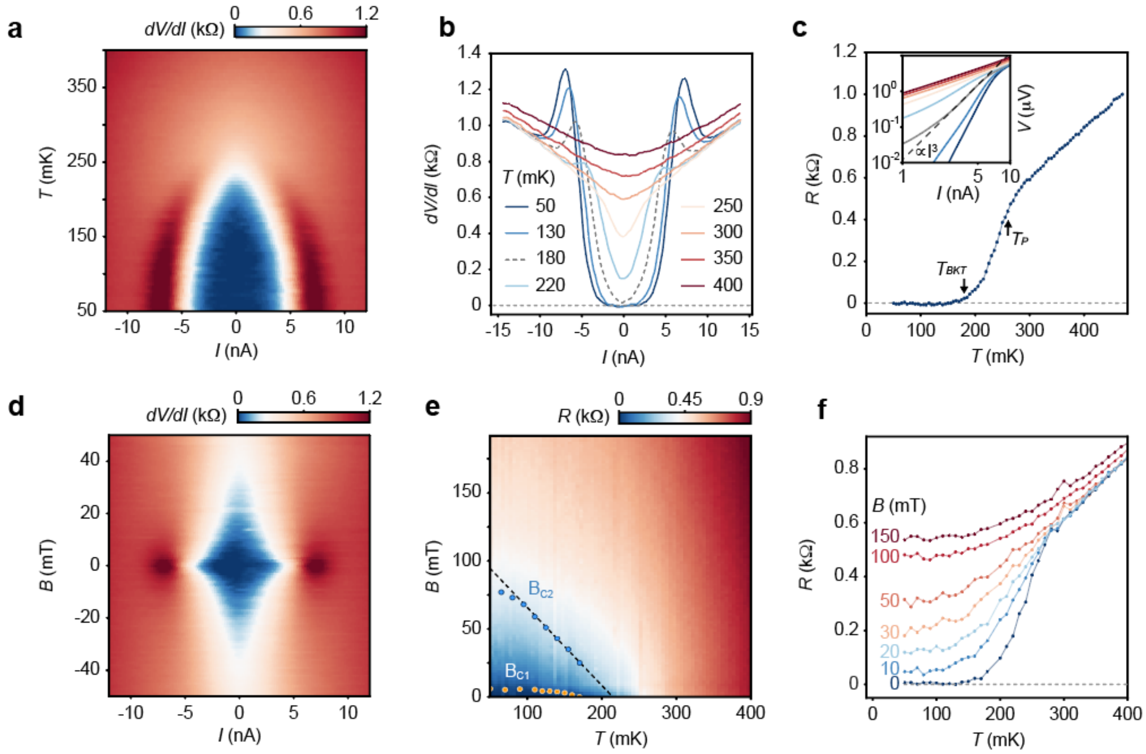

Figure 3 | Superconductivity at half-band filling. a, Differential resistance, $\frac{dV}{dI}$, as a function of temperature T and bias I under zero applied magnetic field. **b,** Linecuts of **a** at representative temperatures. The critical current vanishes continuously with increasing temperature. Dashed line: differential resistance at the BKT transition ($T_{BKT} \approx$180 mK). **c,** Temperature dependence of zero-bias resistance R with two temperature scales, T_{BKT} and T_P. Inset: at T_{BKT}, the V-I dependence follows $V \propto I^3$ (dashed line); the line color is defined in **b**. At $T_P (\approx 250$ mK), R reaches about 80% of the normal-state resistance. **d,** Differential resistance as a function of B and I at 50 mK. The critical current vanishes continuously with increasing magnetic field. **e,** Zero-bias resistance R as a function of B and T with critical field B_{C1} and B_{C2}. The dashed line is a fit of $B_{C2} \approx \frac{B}{2\pi\xi^2}\left(1 - \frac{T}{T_P}\right)$ to data, from which the superconducting coherence length $\xi \approx 52$ nm is determined. **f,** Linecuts of **e** at representative magnetic fields. All data in Fig. 3 are obtained for $\nu \approx 1$ and $E \approx 8$ mV/nm.

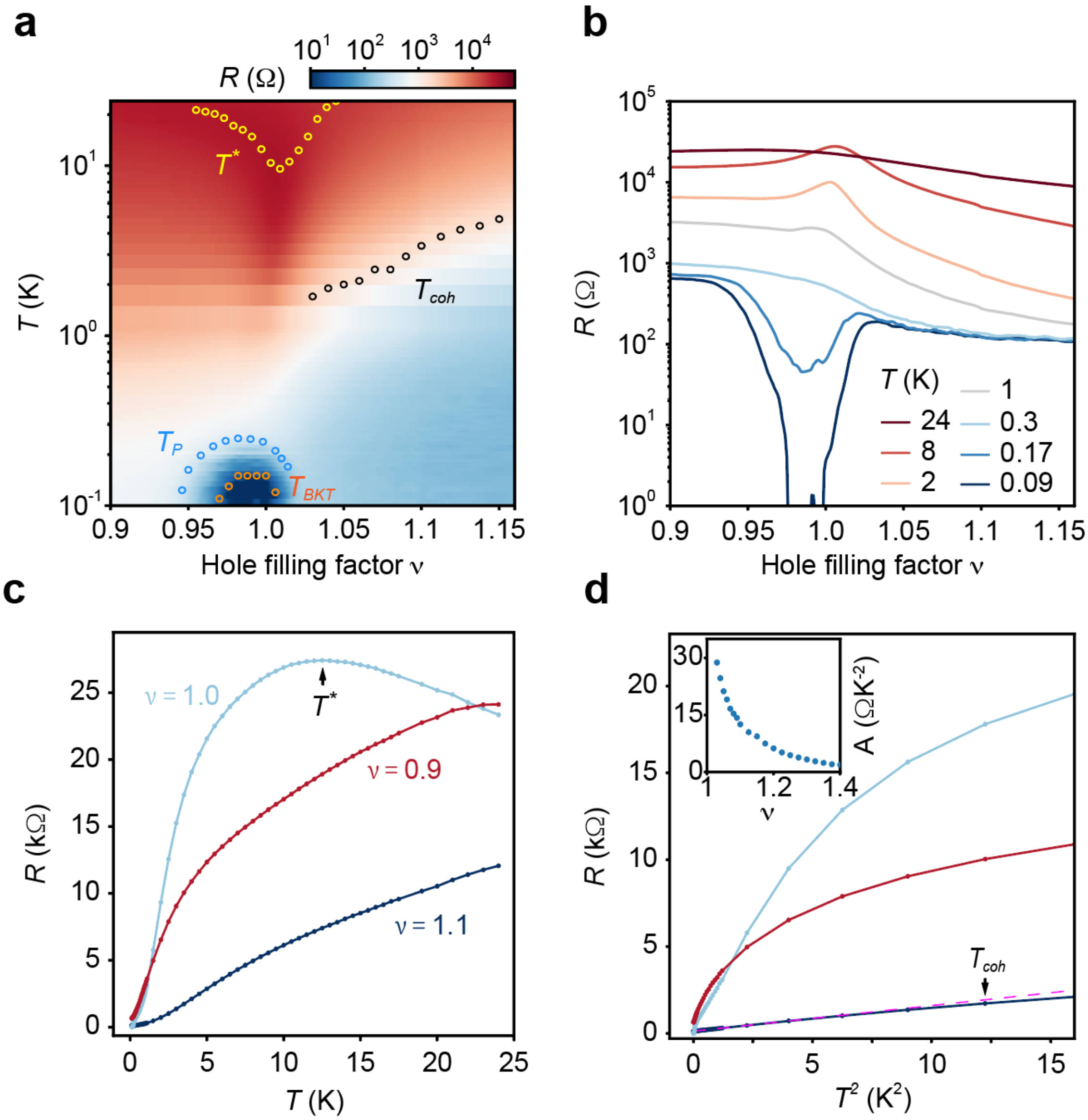

Figure 4 | Doping dependence of the superconducting state. a, Zero-bias resistance R as a function of T and ν at $E \approx 8$ mV/nm and $B = 0$. Superconductivity is observed only near $\nu = 1$. The corresponding normal state shows a resistance peak around 10 K. **b,c,** Linecuts of **a** at representative temperatures (**b**) and filling factors (0.9, 1.0 and 1.1) (**c**). In **c**, T^* denotes the temperature corresponding to the resistance maximum. **d,** Same as **c** up to 4 K displayed as a function of T^2. The dependence for $\nu > 1$ is described by $R = R_0 + AT^2$ (dashed line), where residual resistance R_0 and coefficient A are free parameters. At T_{coh}, R deviates from the T^2-dependence by 10%. Inset: filling dependence of A.

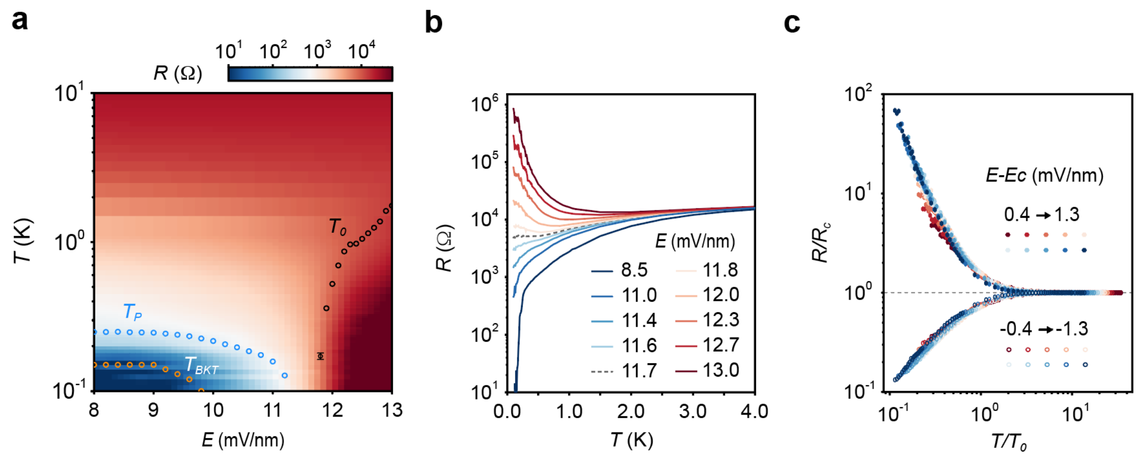

Figure 5 | Superconductor-to-insulator transition. a, Zero-bias resistance R as a function of T and E at $\nu \approx 1$ under zero magnetic field. **b,** Linecuts of **a** at representative electric fields. A superconductor-insulator transition is observed near critical field $E_C \approx 11.7$ mV/nm, at which resistance R_C has the weakest temperature dependence (dashed line). **c,** Collapse of normalized resistance R/R_C into two groups after scaling T by T_0. Here T_0 is the thermal activation temperature extracted from experiment for each $E > E_C$; the same value of T_0 is used for scaling for $E < E_C$ with the same distance to E_C. The colors denote different electric fields measured from E_C with a step size of 0.1 mV/nm; the filled and empty symbols denote E above and below E_C, respectively.

Extended Data Figures

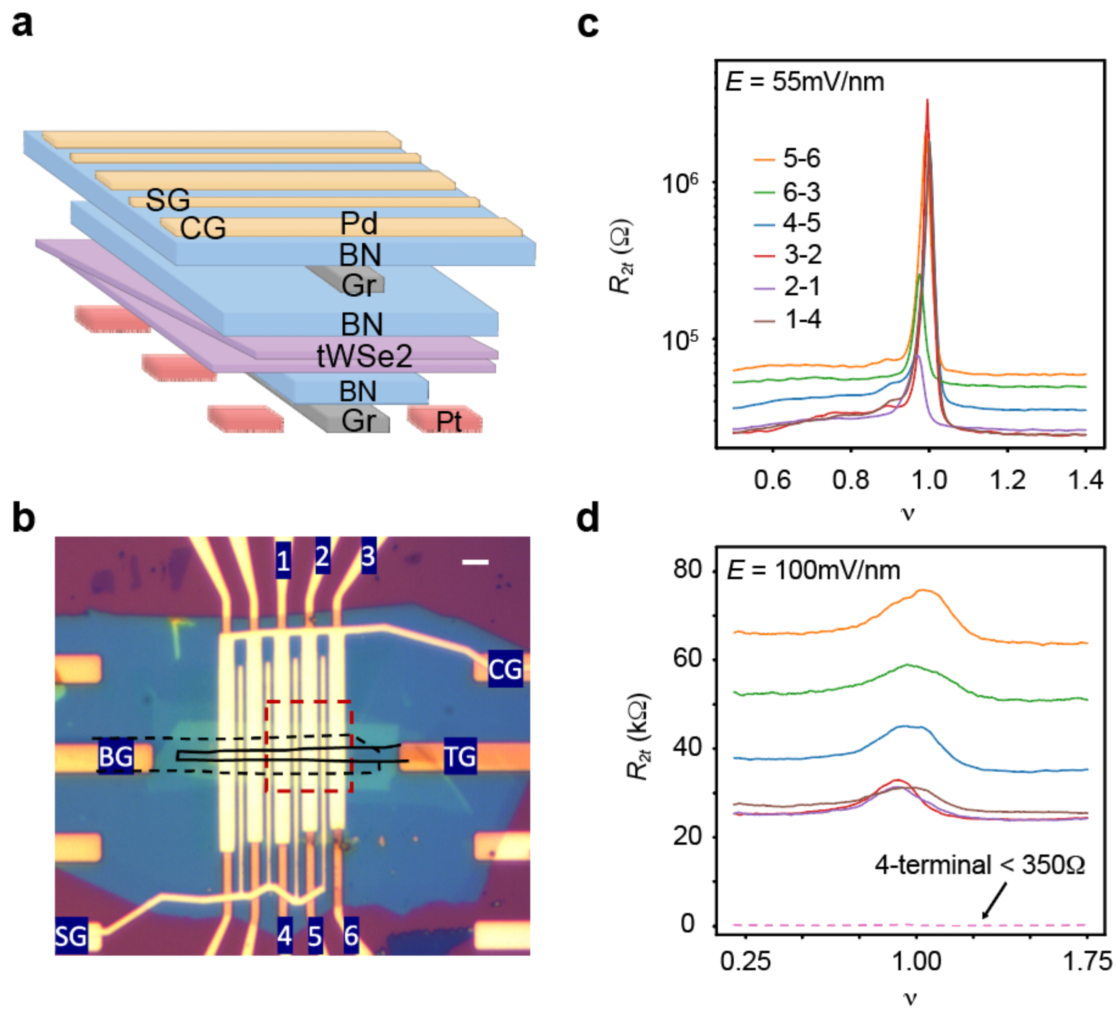

Extended Data Figure 1 | Sample and device characterization. a, Three-dimensional schematic of a $tWSe_2$ dual-gated device. Both the top gate (TG) and bottom gate (BG) are made of hBN and few-layer graphite (Gr). The $tWSe_2$ sample is contacted by Pt electrodes. The Pd contact gates (CG) and split gates (SG) turn on the Pt contacts and turn off the parallel channels, respectively. **b,** Optical micrograph of the 3.65° device. Specific features of interest are BG (enclosed by the black dashed line), TG (black solid line), uniform moiré region (red dashed line) and Pt contact electrode 1-6. The scale bar is 4 µm. **c,d,** Filling factor dependence of two-terminal resistance R_{2t} for different contact pairs at T = 1 K and B = 0 T. The sample is an insulator at $\nu \approx 1$ for E = 55 mV/nm (**c**). The variation in filling factor for the resistance peak is about 0.025, which corresponds to a disorder density of 1×10^{11} cm^{-2} . The sample is a metal at $\nu \approx 1$ for E = 100 mV/nm (**d**) and the four-terminal resistance is below 350 Ω. The contact resistance is determined from R_{2t} to be 10-40 kΩ.

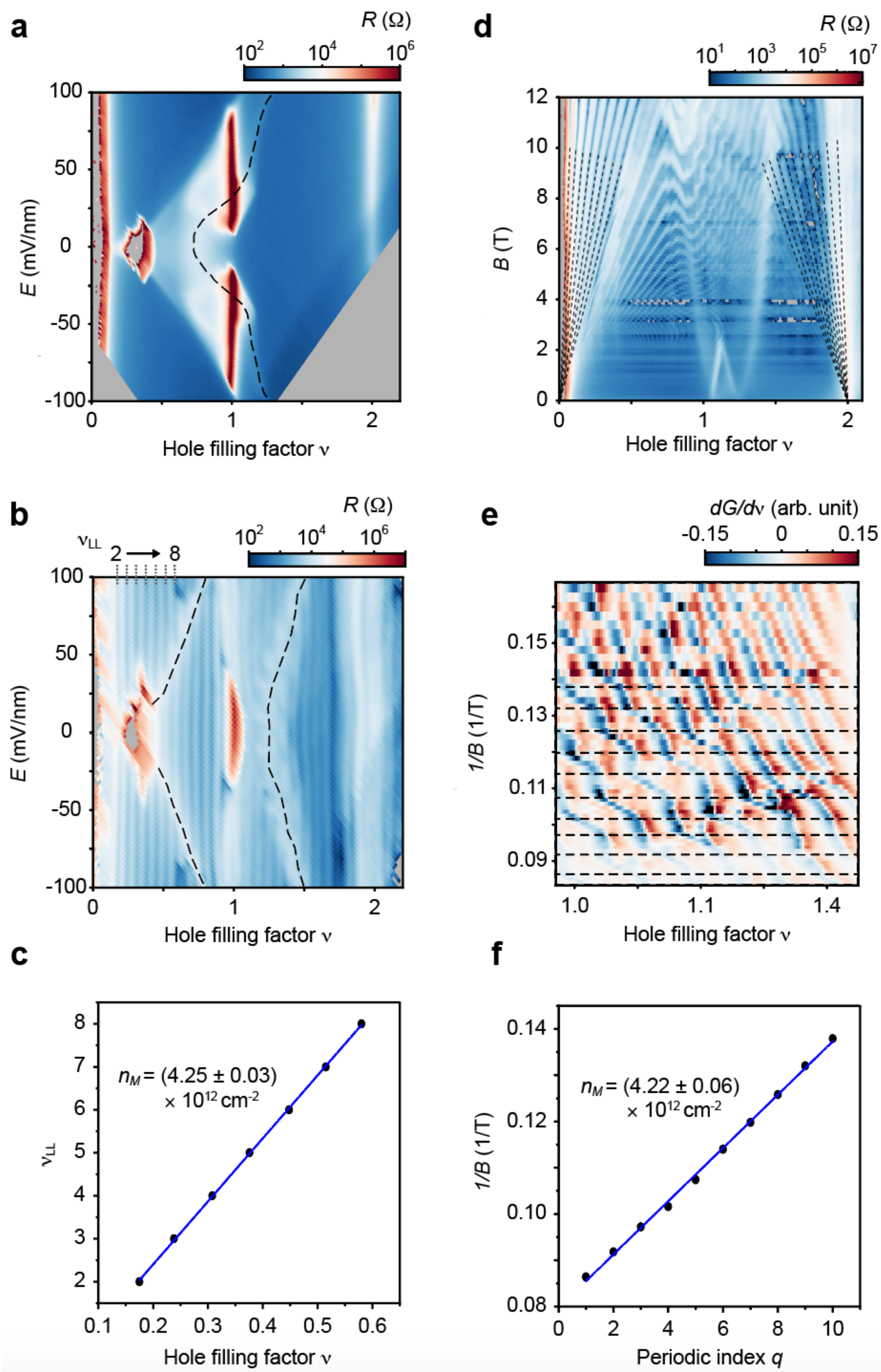

Extended Data Figure 2 | Calibration of the moiré density. a,b, Longitudinal resistance R as a function of E and ν at 50 mK under $B = 0$ T (**a**) and 12 T (**b**). Large bias current is used in the measurement and superconductivity is not observed in **a**. Landau levels are clearly observed in **b**. Landau levels with index $\nu_{LL} = 2 - 8$ (denoted by dotted lines) in the layer-polarized region are spin- and valley-polarized (i.e. nondegenerate). In addition, the Zeeman-split vHS features under $B = 12$ T are marked by dashed lines; these features interrupt the quantum oscillations (the vertical stripes in **b**). The midpoint of the Zeeman-split features is in good agreement with the location of the single vHS feature under $B = 0$ T (dashed line in **a**). **c,** Landau level index ν_{LL} as a function of moiré lattice filling ν follows a linear dependence (blue line). The moiré density is determined from the slope to be $n_M \approx (4.25 \pm 0.03) \times 10^{12}$ cm^{-2}. **d,** R as a function of B and ν at 50 mK and E = 100mV/nm. Two sets of Landau fan emerging from the moiré band edges (i.e. $\nu = 0$ and $\nu = 2$) are marked by the dashed lines. The results give the same moiré density as above. **e,** The derivative of the sample conductance with respect to ν ($dG/d\nu$) as a function of ν and $1/B$ at 50 mK and E = 100mV/nm. Hofstadter's oscillations are observed as periodic crossings of Landau levels in $1/B$, as denoted by the horizontal dashed lines. **f,** $1/B$ at the dashed lines in **e** as a function of the periodic index q. A linear fit to the data gives a $1/B$ period $0.0058 \pm 0.0001 T^{-1}$, which corresponds to $n_M \approx (4.22 \pm 0.06) \times 10^{12}$ cm^{-2}. The value is in good agreement with that obtained from **a-c**.

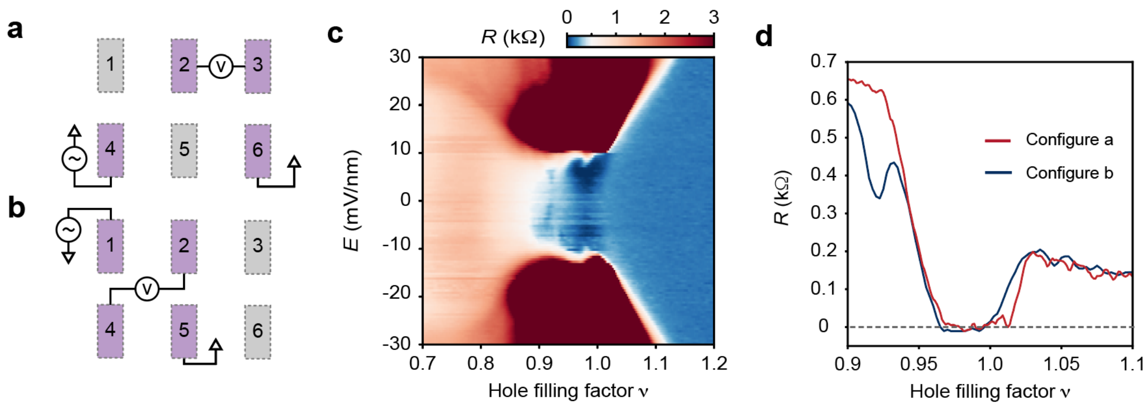

Extended Data Figure 3 | Superconductivity in different measurement configurations. a,b, Measurement configuration for four-terminal resistances: $R_{46,23}$ (**a**) and $R_{15,24}$ (**b**). A bias current is applied on the first two electrodes and the voltage drop is measured using the second two electrodes. The electrodes are labelled as in Extended Data Fig. 1b. Results in the main text are obtained using configuration **a**. **c,** Longitudinal resistance R as a function of E and ν at 50 mK and zero magnetic field using configuration **b**. **d,** Filling dependence of longitudinal resistance R for measurement configuration a and b at $E \approx 8$ mV/nm and $T = 50$ mK. Independent of the measurement configuration, superconductivity is observed in $tWSe_2$ near $\nu = 1$.

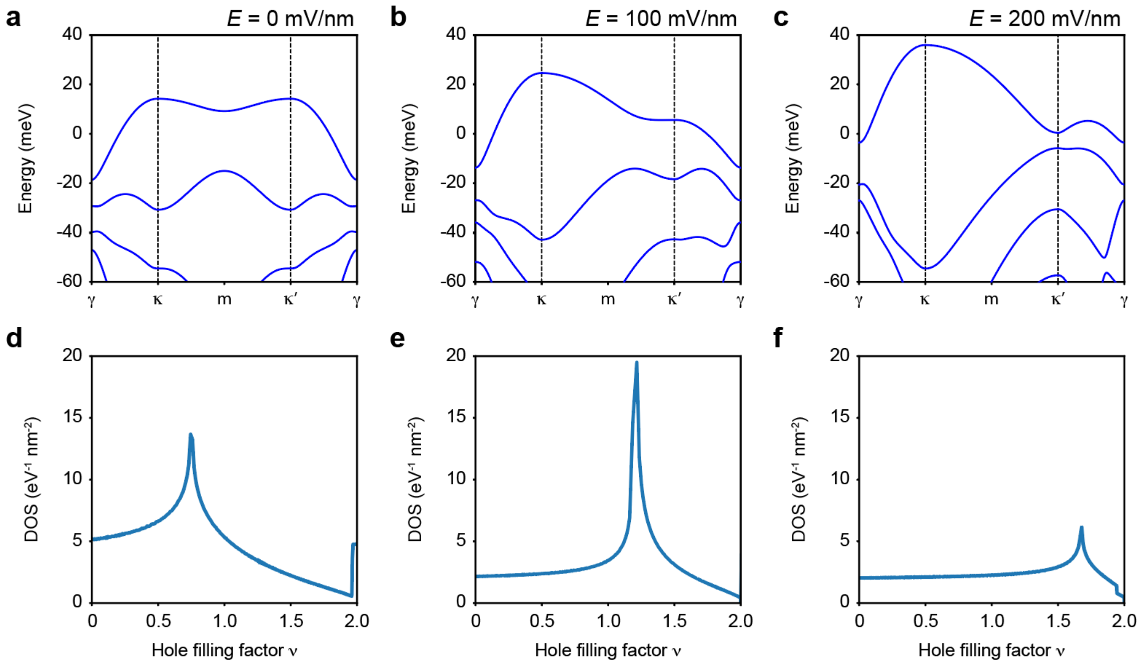

Extended Data Figure 4 | Electronic band structure of 3.65°-tWSe_2 from the continuum model. a-c, Topmost moiré valence bands of the K-valley state for E = 0 mV/nm (**a**), 100 mV/nm (**b**) and 200 mV/nm (**c**). **d-f,** The corresponding electronic DOS as a function of filling ν for the first moiré band. The vHS moves from $\nu < 1$ at $E = 0$ mV/nm to $\nu > 1$ at E = 200 mV/nm. The non-monotonic electric field dependence of DOS at the vHS is dependent on the lifetime broadening we include in the calculations.

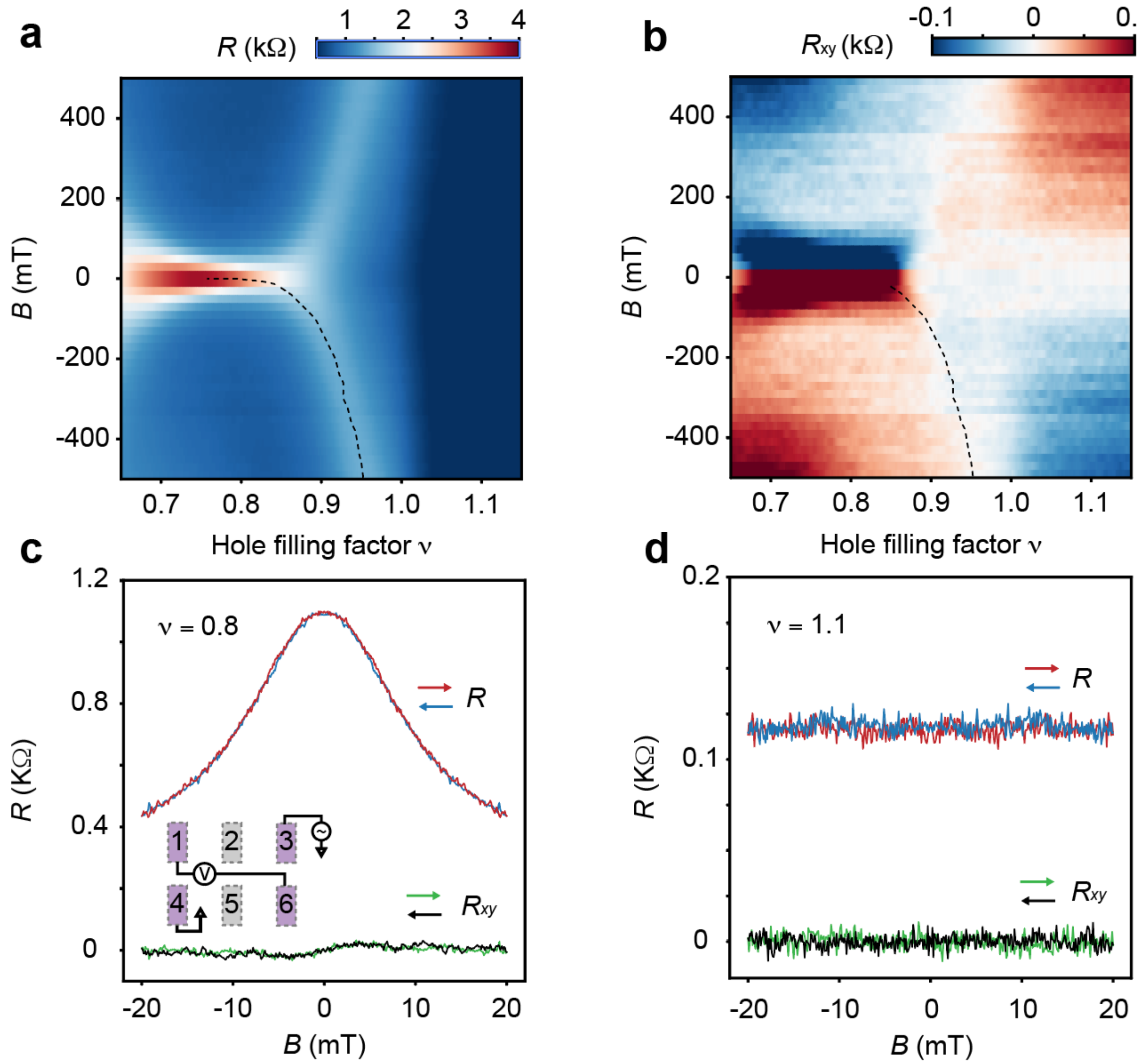

Extended Data Figure 5 | Hall resistance. a,b, Longitudinal resistance R (**a**) and Hall resistance R_{xy} (**b**) as a function of B and ν at T = 50 mK and $E = 0$ mV/nm. Large bias (above the critical current) is applied, and superconductivity is not observed. The strong R_{xy} response below filling 0.9 under small magnetic fields is an artifact because of the large magneto resistance and the coarse field step. The vHS manifests a peak in R (**a**) and a sign change in R_{xy} (**b**). The dashed lines are a guide to the eye of the location of the vHS for negative magnetic fields. The vHS is located at $\nu < 1$ for $B = 0$ and rapidly disperses with B likely due to the combined Zeeman and orbital effects. **c,d,** Linecut of **a,b** at ν = 0.8 (**c**) and ν = 1.1 (**d**) with fine field scans. The measurement configuration is shown in the inset. We symmetrize and anti-symmetrize the response under positive and negative fields to obtain R and R_{xy}, respectively. Both forward and backward field scans are displayed. Magnetic hysteresis is not observed. Anomalous Hall effect is also not observed ($R_{xy} = 0$). The artifact in **b** is removed under fine field scans.

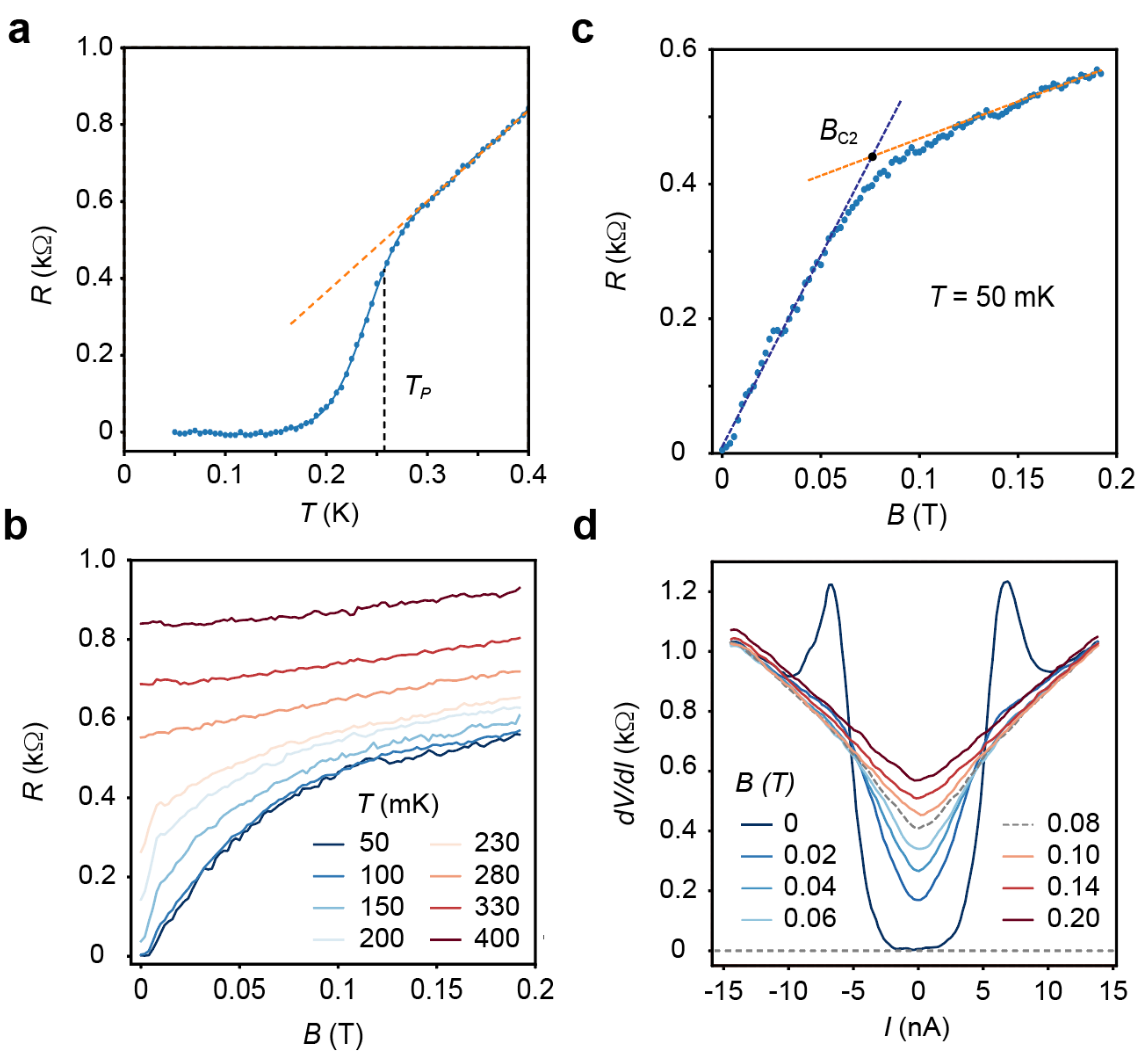

Extended Data Figure 6 | Determination of T_P and B_{c2}. a, Temperature dependence of the zero-bias resistance R at $\nu \approx 1$ ($E \approx 8$ mV/nm and $B = 0$). The pairing temperature T_P (≈ 250 mK, vertical dashed line) is defined as the temperature, at which the measured resistance (blue line) deviates from the projected normal-state resistance (orange line) by 20%. Blue line: polynomial fit to the data (symbols); orange line: linear fit to the normal-state resistance ranging from 300-400 mK. **b**, Magnetic-field dependence of the longitudinal resistance R at differing temperatures ($\nu \approx 1$ and $E \approx 8$ mV/nm). **c,** Magnetic-field dependence of R at 50 mK. The critical field B_{c2} (≈ 80 mT) is defined as the magnetic field, at which the orange and black dashed lines cross. Here the orange line is a linear fit to the normal-state resistance, and the black line is a fit of the unpinned vortex model, $R \propto \frac{B}{B_{C2}}$, to experiment for $B < B_{C2}$. **d,** Bias dependence of the differential resistance $\frac{dV}{dI}$ at varying magnetic fields ($\nu = 1$, $E \approx 8$ mV/nm and $T = 50$ mK*)*. The dashed line corresponds to B_{c2}.

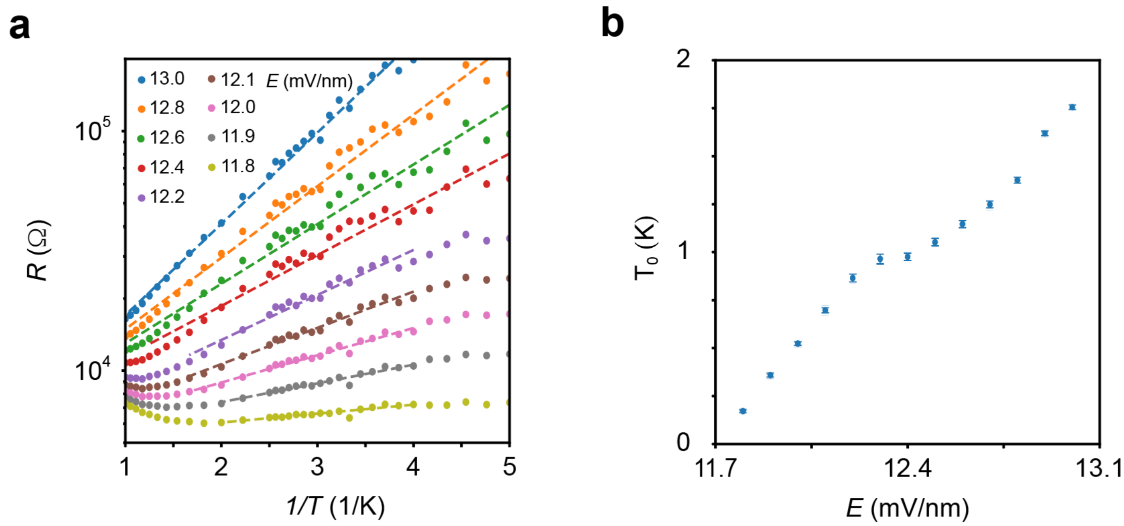

Extended Data Figure 7 | Thermal activation analysis. a, Arrhenius plot of the longitudinal resistance R at varying E (for $\nu = 1$ and $B = 0$). The dashed lines show the thermal activation fit and the range of data where the fit is good. **b,** Extracted gap size T_0 from **a** as a function of E near $E_C \approx 11.7$ mV/nm. The gap vanishes continuously as E approaches E_C from above.

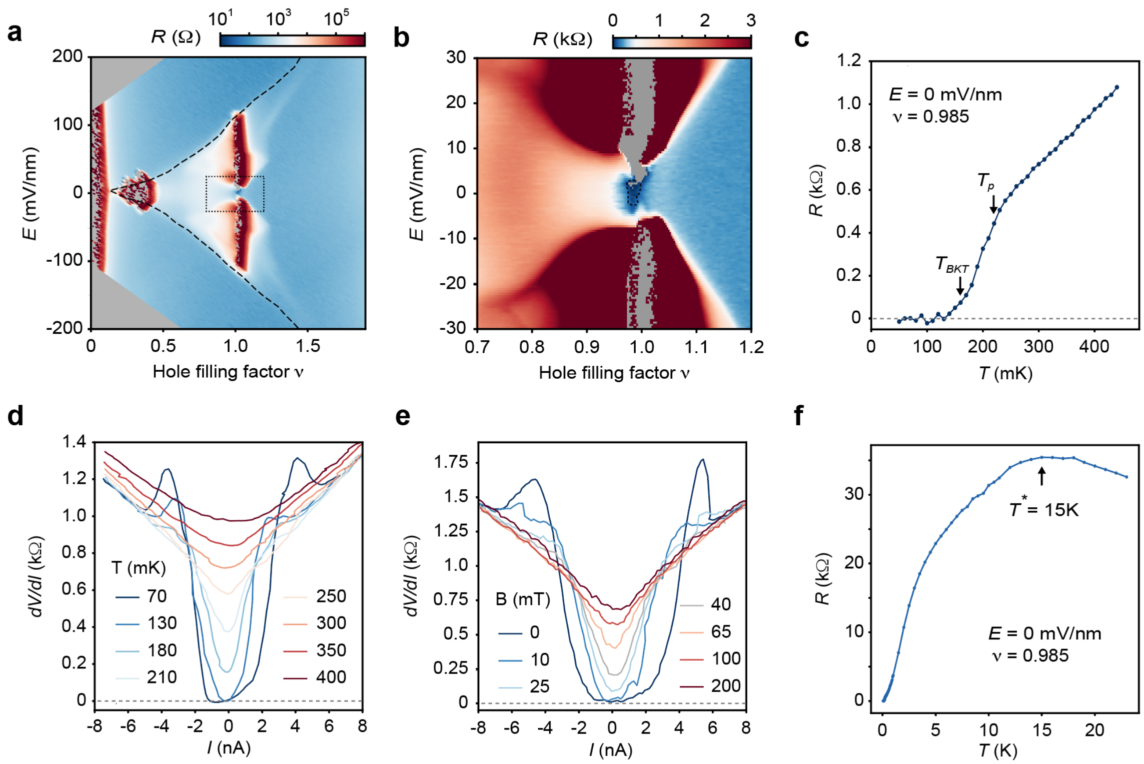

Extended Data Figure 8 | Superconductivity in a 3.5° device. a,b, Longitudinal resistance R as a function of E and ν at 50 mK; **b** shows a zoom-in view of the boxed region in **a**. The dashed lines in **a** (a guide to the eye) separate the layer-hybridized and layer-polarized regions. The dotted lines in **b** are a guide to the eye of the zero-resistance region observed at 50 mK. **c,** Temperature dependence of zero-bias resistance R with two temperature scales, T_{BKT} ≈160 mK and T_P ≈ 210 mK. In contrast to the 3.65° device, the state at $E = 0$ mV/nm is now a superconductor. **d,** Differential resistance, $\frac{dV}{dI}$, as a function of bias Iat different temperatures under zero applied magnetic field. The critical current vanishes continuously with increasing temperature. **e,** Differential resistance as a function of I under different magnetic fields at 50 mK. The critical current vanishes continuously with increasing magnetic field. **f,** Temperature dependence of zero-bias resistance R over a broad temperature range showing the temperature scale T^*.

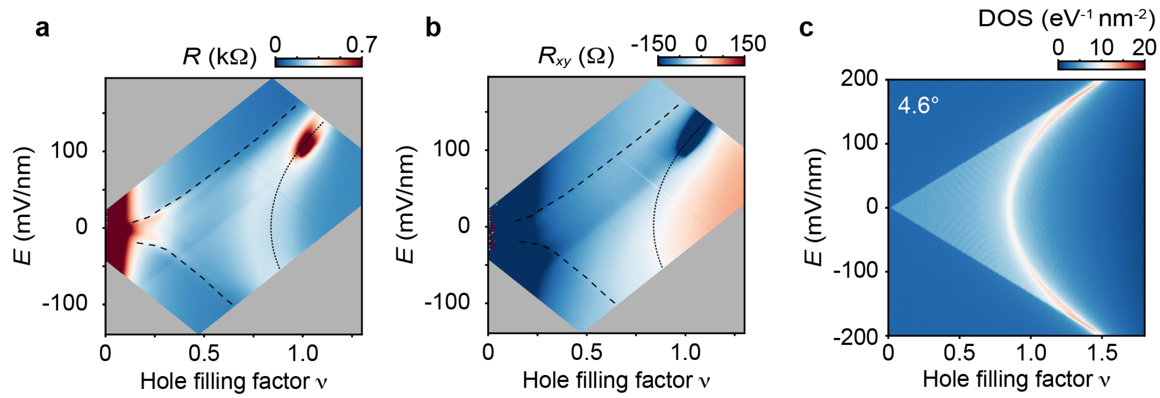

Extended Data Figure 9 | Van Hove singularity in a 4.6-degree device. a,b, Longitudinal resistance R (**a**) and weak-field Hall resistance R_{xy} (**b**) as a function of E and ν at 1.5 K under $B = 0.5$ T. No correlated insulating state is observed at $\nu = 1$ in this twist angle. The dotted line traces the vHS, where R shows a peak and R_{xy} changes sign. The dashed lines separate the layer-hybridized and layer-polarized regions. **c,** Electronic DOS versus E and ν. The vHS ($\nu \approx 0.84$ at $E = 0$) disperses towards higher ν with increasing E. The result is in good agreement with experiment.

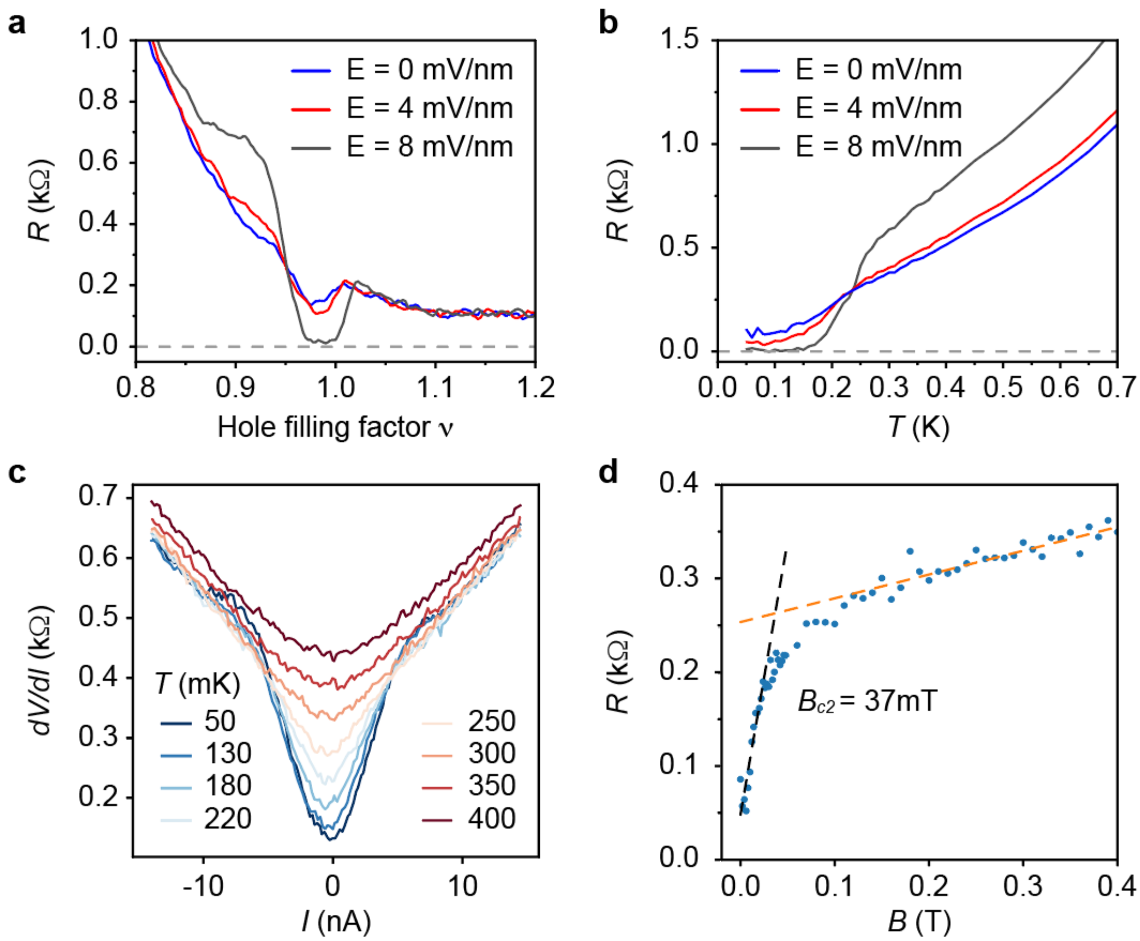

Extended Data Figure 10 | Absence of superconductivity at $E = 0$ mV/nm for the 3.65° device. a, Filling factor dependence of R at varying electric fields at 50 mK. A suppressed but finite resistance is observed at $\nu \approx 1$ and $E = 0$ mV/nm. **b,** Temperature dependence of R at $\nu \approx 1$ and varying electric fields. R at $E = 0$ mV/nm continuously decreases with decreasing temperature. **c,** Differential resistance, $\frac{dV}{dI}$, as a function of bias I at varying temperatures ($\nu \approx 1$ and $E = 0$ mV/nm). A zero-bias $\frac{dV}{dI}$ dip is observed at temperatures below about 250 mK but zero-resistance is not achieved. **d,** Magnetic-field dependence of R at 50 mK ($\nu \approx 1$ and $E = 0$ mV/nm). The critical field B_{c2} (≈ 37 mT) is defined as the magnetic field, at which the orange and black dashed lines cross. The results suggest that the $E = 0$ mV/nm state is either a superconductor with lower T_C than the base electronic temperature of our dilution fridge or a failed superconductor.

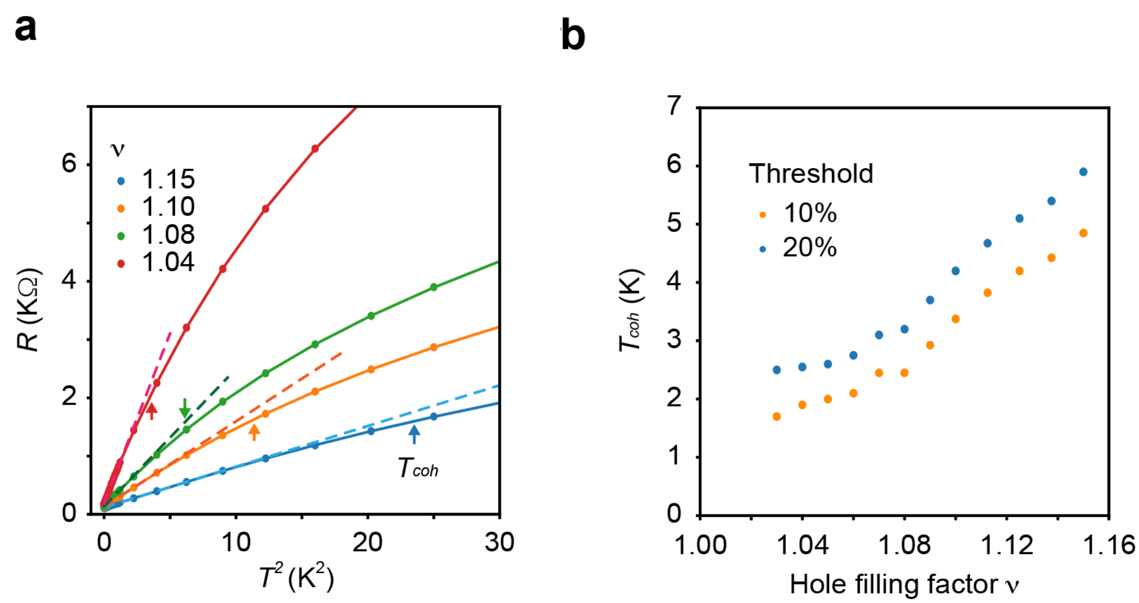

Extended Data Figure 11 | Determination of $\boldsymbol{T_{coh}}$. **a,** R as a function of T^2 at varying filling factors for $\nu > 1$. The dependence at low temperatures is described by $R = R_0 + AT^2$ (dashed line). At T_{coh}, R deviates from the T^2-dependence by 10% (arrows). The solids lines are polynomial fits to the data points. **b,** Filling factor dependence of T_{coh} using 10% and 20% thresholds. The general trend is the same for the two thresholds.